Implementation and Linearization of State-Space Free-Vortex Wake Models for Rotary- and Flapping-Wing Vehicles

Umberto Saetti*
Assistant Professor
Department of Aerospace Engineering
University of Maryland
College Park, MD

Joseph F. Horn
Professor
Department of Aerospace Engineering
Pennsylvania State University
University Park, PA

This work is licensed under Creative Commons Attribution International License CC-BY

This article describes the implementation and linearization of free-vortex wake models in state-variable form as applied to rotary- and flapping-wing vehicles. More specifically, the wake models are implemented and tested for a UH-60 rotor in forward flight and for a hovering insect representative of a hawk moth. A periodic solution to each wake model is found by time marching the coupled rotor/wing and vortex wake dynamics. Next, linearized harmonic decomposition models are obtained and validated against nonlinear simulations. Order reduction methods are explored to guide the development of linearized wake models that provide increased runtime performance compared to the nonlinear and linearized harmonic decomposition wake models while guaranteeing satisfactory prediction of the periodic response of the wake. This constitutes a first attempt to extend free-vortex wake methods in state-variable form, originally developed for rotary-wing applications, to flapping-wing flight.

Introduction

Simulations of rotorcraft flight dynamics have advanced significantly over the past decade. To provide rapid simulations of generalized maneuvering flight, flight dynamic models were once restricted to relatively low-fidelity aeromechanics models, for example, finite-state inflow, rigid blade element models. On the other hand, comprehensive aeromechanics simulations historically used much higher fidelity aeromechanics, for example, free vortex–wake modeling or even computational fluid dynamics (CFD) coupled with structural dynamics, at the cost of longer run times with analysis restricted to trim or very simple maneuvers. But in recent years, increasingly higher fidelity aeromechanics are making their way into flight dynamics simulations, and even real-time pilote d simulations. Real-time time-accurate free wake modeling was implemented in the General Helicopter (GenHel) (Ref. 1) simulation and demonstrated using the CHARM Wake Module (Ref. 2) in the early 2000s. The CHARM Wake Module was subsequently implemented in Navy training simulators coupled with ship airwake effects (Ref. 3). FLIGHTLAB has the capability to use viscous vortex particle models (VVPM) (Ref. 4). Both free wake and VVPM models have the capability to predict rotor inflow and rotor wake interference effects in generalized maneuvering flight, moving beyond simplified models and empirical models that have been historically used in flight simulations. In 2017, Ref. 5 even investigated the feasibility of using Euler-based CFD methods in real-time simulation models. While those results indicated that such an approach is theoretically possible, the CFD would need to be greatly simplified and rely on massively parallelized computations. In any case, the gap between the fidelity of rotorcraft flight simulation models and rotorcraft comprehensive models is steadily closing.

In the meantime, new configurations have become more complex. Future vertical lift and urban air mobility (UAM) configurations feature multiple rotors, high levels of aerodynamic interactions, and in the case of UAM, high RPM/variable speed rotors. These features drive the need for advanced aeromechanics models while at the same time making real-time simulation (or even sufficiently fast execution speeds for routine design) much more difficult. For example, time steps in rotor models are driven by the minimum blade sweep per time step, so computational cost goes up with smaller, higher RPM rotors. Modeling aerodynamic interactions requires larger amounts of wake to be computed, and rigid rotor systems require more costly structural dynamics models of the blades. Thus, while more advanced aeromechanics models are feasible, it is likely that in many cases, execution speeds required for real-time simulations or routine design applications will remain elusive.

With regard to biological flyers (insects and birds), and their man-made counterparts, flapping-wing micro aerial vehicles (FWMAVs), their flight dynamics is typically challenging to both model and analyze. Challenges emanate from their multibody, nonlinear, and time-varying nature of such dynamical systems. In fact, the dynamics of flapping flight is described by nonlinear time-periodic (NLTP) systems of the coupled rigid-body and complex interactional aerodynamics between the wings, body, and the self-induced wake. To be representative of the coupled

*Corresponding author: Umberto Saetti; email: saetti@umd.edu.
Manuscript received May 2022; accepted March 2023.

 © 2023 Vertical Flight Society

rigid-body and complex interactional aerodynamics between the wings, body, and the self-induced wake and at the same time being suited to time-periodic systems analysis, simulations of flapping-wing vehicles will require high-fidelity aerodynamics models that are also in state-space form. While flight dynamics models that included state-space representations of the unsteady flapping aerodynamics exist and were derived both from physics-based models (see, *e.g.*, Refs. 6, 7) or using data-driven approaches (see, *e.g.*, Refs. 8), these models are very low order and do not account for the wake geometry and its interaction with itself and the insect body. On the other hand, high-fidelity aeromechanics models do exist for flapping-wing flight (see, *e.g.*, Refs. 9–13) but are either not expressed in, or suited for, state-space formulation and thus cannot be used to derive self-contained coupled linearized models of the flight dynamics and interactional wing-body-wake aerodynamics for use in stability analysis and control design.

It is therefore critical for both rotary- and flapping-wing applications that high-fidelity aeromechanics models are formulated in such a way that they can be readily linearized and/or simplified to extract more tractable and less expensive models. Linearized state-space models are particularly attractive from the control designers perspectives. Not only are linearized models used in a majority of practical control design methodologies, but linear model analysis provides many physical insights into system dynamics. To this end, a first-order state variable implementation of the aeromechanics (or state-space implementation) that can be efficiently linearized is a highly desirable feature for future advanced simulations.

There have been some recent efforts to extract linearized state-space models from free-wake and VVPM models using system identification methods (Refs. 14,15). These approaches perform frequency sweep excitations on the rotor wake model, then perform frequency domain system identification to extract a low-order linearized model. These are in the form of finite-state inflow models and thus can be readily employed in simulation models. The method has the advantage that it can be applied to almost any wake model, and the wake model does not need to be in state variable form. However, it is not a self-contained or automated process. Frequency sweeps need to be generated across the range of flight conditions of interest, and the system identification process needs to be performed and checked for each of these flight conditions.

In Ref. 16, a state-space free-wake model is introduced in which the method of lines is used to express the partial differential equations (PDEs) constituting the University Maryland Free Wake Model (Refs. 17,18) into the first-order state variable form. The formulation of the Maryland Free Wake model is well-suited for state space implementation due to the introduction of the wake age parameter, such that a particular wake state represents the position of a free wake node of a given age. The wake age is an angular distance measured along the vortex starting from the vortex release point on the wing/blade trailing edge. The underlying PDEs are governed by the Biot–Savart law, which is the most expensive part of the free-wake computation. These PDEs are discretized with respect to the wake age using a fourth-order five-point biased upwind (5PBU4) scheme. The discretized system becomes a set of first-order ODEs in time (*i.e.*, a state-space system) which can be accurately integrated forward in time and linearized. This wake model consisted of only the wake node positions. The vortex strength was not considered in the systems state so presumably vortex strength is constant along the filament.

There are two major challenges to linearizing wake models: (i) the wake states are inherently periodic in equilibrium and (ii) the number of wake states can be quite large (in the order of several thousands of states) such that numerical perturbations of all states become expensive. One approach is to average the effect of perturbations over a single revolution/wing beat cycle (Refs. 19–27), but a more rigorous approach is to generate a linear time-periodic (LTP) model by generating linear models across a range of azimuth/flapping angle positions. One then has

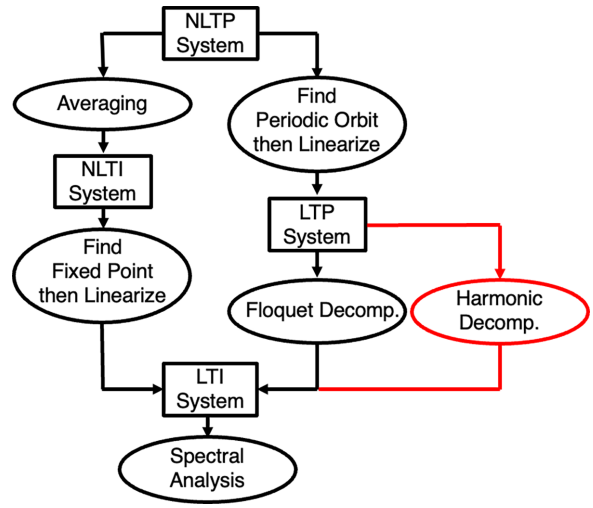

Fig. 1. Illustration of the two main approaches to stability analysis of NLTP systems: averaging methods (left), Floquet theory, and harmonic decomposition (right).

the option to extract an LTP model, convert this LTP model to linear time-invariant (LTI) through averaging, or extract a harmonic decomposition model (Refs. 28, 29). These two main approaches to NLTP system stability analysis are shown qualitatively in Fig. 1. Recently, the harmonic decomposition method (Ref. 28) was adopted to represent LTP systems with higher order LTI models for use in prediction of loads and vibration in a control design framework (Ref. 30–32). While harmonic decomposition originated from within the rotorcraft community, it was also recently extended to flapping-wing flight (Ref. 33). The major advantage of harmonic decomposition is that, unlike previous methods such as the Lyapunov–Floquet method (Ref. 34) and frequency lifting methods (Ref. 35), it does not rely on state transition matrices. In fact, state transition matrices constitute a particular challenge in that their computation can be time-intensive and/or numerically very sensitive. Additionally, when coupled with a harmonic balance scheme, harmonic decomposition can also be used to compute: (i) periodic solutions to the system dynamics, and open- and closed-loop control laws to abate arbitrary state/output harmonics (Ref. 36). Still, the cost of linearization also needs to be addressed. For example, in Ref. 37, a VVPM model was linearized within the rotorcraft comprehensive analysis system (RCAS) framework, which formulates dynamics as second-order implicit state equations. The authors noted that the cost of running the implicit equations to a steady state for each numerical perturbation was very high. Instead, they applied simplified numerical perturbations in the form of a finite-state inflow to extract reduced order linear models.

As such, the objectives of the proposed investigation are threefold. The first objective is to develop a state variable implementation of a free-vortex wake model that is suitable for both rotary- and flapping-wing applications. Additionally, this model will have to be self-contained and inherently linearizable and thus does not require external processing to generate approximate linear models. The second objective is to demonstrate the linearization of this high-fidelity aeromechanics model. The third objective is to investigate model-order reduction methods to guide the development of simplified models with increased runtime performance while still capturing the underlying physics of the original dynamics.

The article begins with a discussion of the mathematical background behind NLTP systems and the corresponding linearization and model-order reduction methods. State-space free vortex wake models are presented in the context of rotary-wing and flapping-wing vehicles. This

is followed by results on the implementation and validation of the free-vortex wake model as applied to a blade element representation of a UH-60 rotor in forward flight and to a hovering insect representative of a hawk moth. Next, linearized models of the coupled rotor/wing and free-vortex wake dynamics are obtained and tested against nonlinear simulations. Reduced-order models are also investigated. Final remarks summarize the overall findings of the study.

Methodology

Mathematical background

Consider an NLTP system in the first-order form representative of the free-vortex wake dynamics of rotary- or flapping-wing vehicles:

$$\dot{\boldsymbol{x}} = \boldsymbol{f}(\boldsymbol{x}, \boldsymbol{u}, t) \tag{1a}$$

$$\boldsymbol{y} = \boldsymbol{g}(\boldsymbol{x}, \boldsymbol{u}, t) \tag{1b}$$

where $\boldsymbol{x} \in \mathbb{R}^n$ is the state vector, $\boldsymbol{u} \in \mathbb{R}^m$ is the control input vector, $\boldsymbol{y} \in \mathbb{R}^l$ is the output vector, and t is the dimensional time in seconds. The nonlinear functions $\boldsymbol{f}$ and $\boldsymbol{g}$ are T-periodic in time such that

$$\boldsymbol{f}(\boldsymbol{x}, \boldsymbol{u}, t) = \boldsymbol{f}(\boldsymbol{x}, \boldsymbol{u}, t + T) \tag{2a}$$

$$\boldsymbol{g}(\boldsymbol{x}, \boldsymbol{u}, t) = \boldsymbol{g}(\boldsymbol{x}, \boldsymbol{u}, t + T) \tag{2b}$$

Note that the fundamental period of the system is $T = \frac{2\pi}{\omega}$ seconds, where ω is either the angular speed of the main rotor or the flapping frequency, depending on the vehicle, in radians/second. Let $\boldsymbol{x}^*(t)$ and $\boldsymbol{u}^*(t)$ represent a periodic solution of the system such that $\boldsymbol{x}^*(t) = \boldsymbol{x}^*(t+T)$ and $\boldsymbol{u}^*(t) = \boldsymbol{u}^*(t+T)$. Then, the NLTP system can be linearized about the periodic solution. Consider the case of small disturbances:

$$\boldsymbol{x} = \boldsymbol{x}^* + \boldsymbol{\Delta x} \tag{3a}$$

$$\boldsymbol{u} = \boldsymbol{u}^* + \boldsymbol{\Delta u} \tag{3b}$$

where $\boldsymbol{\Delta x}$ and $\boldsymbol{\Delta u}$ are the state and control perturbation vectors from the candidate periodic solution. A Taylor series expansion is performed on the state derivative and output vectors. Neglecting terms higher than first order results in the following equations:

$$\boldsymbol{f}(\boldsymbol{x}^* + \boldsymbol{\Delta x}, \boldsymbol{u}^* + \boldsymbol{\Delta u}, t) = \boldsymbol{f}(\boldsymbol{x}^*, \boldsymbol{u}^*, t) + \boldsymbol{F}(t)\boldsymbol{\Delta x} + \boldsymbol{G}(t)\boldsymbol{\Delta u} \tag{4a}$$

$$\boldsymbol{g}(\boldsymbol{x}^* + \boldsymbol{\Delta x}, \boldsymbol{u}^* + \boldsymbol{\Delta u}, t) = \boldsymbol{g}(\boldsymbol{x}^*, \boldsymbol{u}^*, t) + \boldsymbol{P}(t)\boldsymbol{\Delta x} + \boldsymbol{Q}(t)\boldsymbol{\Delta u} \tag{4b}$$

where

$$\boldsymbol{F}(t) = \left.\frac{\partial \boldsymbol{f}(\boldsymbol{x}, \boldsymbol{u})}{\partial \boldsymbol{x}}\right|_{\boldsymbol{x}^*, \boldsymbol{u}^*}, \quad \boldsymbol{G}(t) = \left.\frac{\partial \boldsymbol{f}(\boldsymbol{x}, \boldsymbol{u})}{\partial \boldsymbol{u}}\right|_{\boldsymbol{x}^*, \boldsymbol{u}^*} \tag{5a-b}$$

$$\boldsymbol{P}(t) = \left.\frac{\partial \boldsymbol{g}(\boldsymbol{x}, \boldsymbol{u})}{\partial \boldsymbol{x}}\right|_{\boldsymbol{x}^*, \boldsymbol{u}^*}, \quad \boldsymbol{Q}(t) = \left.\frac{\partial \boldsymbol{g}(\boldsymbol{x}, \boldsymbol{u})}{\partial \boldsymbol{u}}\right|_{\boldsymbol{x}^*, \boldsymbol{u}^*} \tag{5c-d}$$

Note that the state-space matrices in Eq. (5) have T-periodic coefficients such that

$$\boldsymbol{F}(t) = \boldsymbol{F}(t+T), \quad \boldsymbol{G}(t) = \boldsymbol{G}(t+T) \tag{6a-b}$$

$$\boldsymbol{P}(t) = \boldsymbol{P}(t+T), \quad \boldsymbol{Q}(t) = \boldsymbol{Q}(t+T) \tag{6c-d}$$

Equations (4a) and (4b) yield an LTP approximation of the NLTP system of Eq. (34) as follows:

$$\boldsymbol{\Delta \dot{x}} = \boldsymbol{F}(t)\boldsymbol{\Delta x} + \boldsymbol{G}(t)\boldsymbol{\Delta u} \tag{7a}$$

$$\boldsymbol{\Delta y} = \boldsymbol{P}(t)\boldsymbol{\Delta x} + \boldsymbol{Q}(t)\boldsymbol{\Delta u} \tag{7b}$$

Hereafter, the notation is simplified by dropping the Δ in front of the linearized perturbation state and control vectors while keeping in mind that these vectors represent perturbations from a periodic equilibrium. Next, the state, input, and output vectors of the LTP systems are decomposed into a finite number of harmonics of the fundamental period via Fourier analysis:

$$\boldsymbol{x} = \boldsymbol{x}_0 + \sum_{i=1}^{N} \boldsymbol{x}_{ic} \cos\left(\frac{2\pi i t}{T}\right) + \boldsymbol{x}_{is} \sin\left(\frac{2\pi i t}{T}\right) \tag{8a}$$

$$\boldsymbol{u} = \boldsymbol{u}_0 + \sum_{j=1}^{M} \boldsymbol{u}_{jc} \cos\left(\frac{2\pi j t}{T}\right) + \boldsymbol{u}_{js} \sin\left(\frac{2\pi j t}{T}\right) \tag{8b}$$

$$\boldsymbol{y} = \boldsymbol{y}_0 + \sum_{k=1}^{L} \boldsymbol{y}_{kc} \cos\left(\frac{2\pi k t}{T}\right) + \boldsymbol{y}_{ks} \sin\left(\frac{2\pi k t}{T}\right) \tag{8c}$$

As shown in Ref. 28, the harmonic decomposition methodology can be used to transform the LTP model into an approximate higher order LTI model in the first-order form:

$$\dot{\boldsymbol{X}} = \boldsymbol{A}\boldsymbol{X} + \boldsymbol{B}\boldsymbol{U} \tag{9a}$$

$$\boldsymbol{Y} = \boldsymbol{C}\boldsymbol{X} + \boldsymbol{D}\boldsymbol{U} \tag{9b}$$

where the augmented state, control, and output vectors $\boldsymbol{X} \in \mathbb{R}^{n(2N+1)}$, $\boldsymbol{U} \in \mathbb{R}^{m(2M+1)}$, and $\boldsymbol{Y} \in \mathbb{R}^{l(2L+1)}$, respectively, are given by:

$$\boldsymbol{X}^T = \begin{bmatrix} \boldsymbol{x}_0^T & \boldsymbol{x}_{1c}^T & \boldsymbol{x}_{1s}^T & \dots & \boldsymbol{x}_{Nc}^T & \boldsymbol{x}_{Ns}^T \end{bmatrix} \tag{10a}$$

$$\boldsymbol{U}^T = \begin{bmatrix} \boldsymbol{u}_0^T & \boldsymbol{u}_{1c}^T & \boldsymbol{u}_{1s}^T & \dots & \boldsymbol{u}_{Mc}^T & \boldsymbol{u}_{Ms}^T \end{bmatrix} \tag{10b}$$

$$\boldsymbol{Y}^T = \begin{bmatrix} \boldsymbol{y}_0^T & \boldsymbol{y}_{1c}^T & \boldsymbol{y}_{1s}^T & \dots & \boldsymbol{y}_{Lc}^T & \boldsymbol{y}_{Ls}^T \end{bmatrix} \tag{10c}$$

with $\boldsymbol{A} \in \mathbb{R}^{n(2N+1) \times n(2N+1)}$, $\boldsymbol{B} \in \mathbb{R}^{n(2N+1) \times m(2M+1)}$, $\boldsymbol{C} \in \mathbb{R}^{l(2L+1) \times n(2N+1)}$, and $\boldsymbol{D} \in \mathbb{R}^{l(2L+1) \times m(2M+1)}$. Closed-form expressions for these matrices can be found in Ref. 28. It is worth noting that harmonic decomposition does not rely on state transition matrices, which makes the methodology more computationally efficient and less numerically sensitive than other approaches such as the Lyapunov–Floquet method (Ref. 34) and frequency lifting methods (Ref. 35).

Model-order reduction

Because the harmonic decomposition models described above may become of very high order depending on the number of states and number of state harmonics retained, they can result in runtime performance significantly slower than real-time. To improve the runtime performance, it is desired to obtain reduced-order models. Not only do reduced-order models yield decreased simulation time, but they also remove the need to measure or estimate the higher harmonic states, which may be challenging or impractical when performing control system design. Ideally, these reduced-order models do not include the higher harmonic states but still retain part of the higher harmonic response characteristics. This can be achieved through residualization, a portion of singular perturbation theory that pertains to LTI systems (Ref. 38). Assuming that one or more states of the system have stable dynamics which are faster than that of the remaining states, the state vector in Eq. (10a) can be partitioned into fast and slow components:

$$\boldsymbol{X}^T = \begin{bmatrix} \boldsymbol{X}_\mathrm{s}^T & \boldsymbol{X}_\mathrm{f}^T \end{bmatrix} \tag{11}$$

Then, the system in Eq. (9a) can be rewritten as

$$\begin{bmatrix} \dot{\boldsymbol{X}}_\mathrm{s} \\ \dot{\boldsymbol{X}}_\mathrm{f} \end{bmatrix} = \begin{bmatrix} \boldsymbol{A}_\mathrm{s} & \boldsymbol{A}_\mathrm{sf} \\ \boldsymbol{A}_\mathrm{fs} & \boldsymbol{A}_\mathrm{f} \end{bmatrix} \begin{bmatrix} \boldsymbol{X}_\mathrm{s} \\ \boldsymbol{X}_\mathrm{f} \end{bmatrix} + \begin{bmatrix} \boldsymbol{B}_\mathrm{s} \\ \boldsymbol{B}_\mathrm{f} \end{bmatrix} \boldsymbol{U} \tag{12}$$

By neglecting the dynamics of the fast states (*i.e.*, $\dot{\boldsymbol{X}}_\mathrm{f} = 0$) and performing a few algebraic manipulations, the equations for a reduced-order

system with the state vector composed of the slow states may be found:

$$\dot{\boldsymbol{X}}_{\mathrm{s}} = \hat{\boldsymbol{A}}\boldsymbol{X}_{\mathrm{s}} + \hat{\boldsymbol{B}}\boldsymbol{U} \tag{13}$$

where

$$\hat{\boldsymbol{A}} = \boldsymbol{A}_{\mathrm{s}} - \boldsymbol{A}_{\mathrm{sf}}\boldsymbol{A}_{\mathrm{f}}{}^{-1}\boldsymbol{A}_{\mathrm{fs}} \tag{14a}$$

$$\hat{\boldsymbol{B}} = \boldsymbol{B}_{\mathrm{s}} - \boldsymbol{A}_{\mathrm{sf}}\boldsymbol{A}_{\mathrm{f}}{}^{-1}\boldsymbol{B}_{\mathrm{f}} \tag{14b}$$

Note that A_f must be invertible. This is guaranteed if A_f is asymptotically stable, that is, all eigenvalues have their real part that is strictly negative. In this study, the slow states are chosen as the zeroth harmonic states, whereas the fast states are taken as the higher harmonics:

$$\boldsymbol{X}_{\mathrm{s}} = \boldsymbol{x}_0 \tag{15a}$$

$$\boldsymbol{X}_{\mathrm{f}}^T = \begin{bmatrix}\boldsymbol{x}_{1c}^T\ \boldsymbol{x}_{1s}^T\ \ldots\ \boldsymbol{x}_{Nc}^T\ \boldsymbol{x}_{Ns}^T\end{bmatrix} \tag{15b}$$

For the residualized model to retain information of the influence or the residualized dynamics on not only the zeroth harmonics of the output but also on its higher output harmonics, consider partitioning the output equations in Eq. (9b) as

$$\boldsymbol{Y} = [\boldsymbol{C}_{\mathrm{s}}\ \boldsymbol{C}_{\mathrm{f}}]\begin{bmatrix}\boldsymbol{X}_{\mathrm{s}}\\ \boldsymbol{X}_{\mathrm{f}}\end{bmatrix} + \boldsymbol{D}\boldsymbol{U} \tag{16}$$

Then, it can be shown that the residualized output equations are

$$\dot{\boldsymbol{Y}} = \hat{\boldsymbol{C}}\boldsymbol{X}_{\mathrm{s}} + \hat{\boldsymbol{D}}\boldsymbol{U} \tag{17}$$

where

$$\hat{\boldsymbol{C}} = \boldsymbol{C}_{\mathrm{s}} - \boldsymbol{C}_{\mathrm{f}}\boldsymbol{A}_{\mathrm{f}}{}^{-1}\boldsymbol{A}_{\mathrm{fs}} \tag{18a}$$

$$\hat{\boldsymbol{D}} = \boldsymbol{D} - \boldsymbol{C}_{\mathrm{f}}\boldsymbol{A}_{\mathrm{f}}{}^{-1}\boldsymbol{B}_{\mathrm{f}} \tag{18b}$$

If now the augmented output vector is selected to coincide with the augmented state vector, such that

$$\boldsymbol{Y}^T = \begin{bmatrix}\boldsymbol{x}_0^T\ \boldsymbol{x}_{1c}^T\ \boldsymbol{x}_{1s}^T\ \ldots\ \boldsymbol{x}_{Nc}^T\ \boldsymbol{x}_{Ns}^T\end{bmatrix} \tag{19}$$

then, the residualized model will be able to predict the influence of the residualized dynamics on the zeroth and higher harmonic states.

Modeling of Rotary and Flapping Wings

Rotor model

The rotor of the PSUHeloSim flight simulation code (Ref. 39) is used as a base for the implementation of the state-space free-vortex wake model. This rotor is representative of the rotor of a notional utility helicopter similar to the UH-60 and is based on Ref. 1. The model contains rigid flap and lead–lag rotor blade dynamics, a three-state Pitt–Peters inflow model (Ref. 40), and nonlinear aerodynamic lookup tables for the rotor blades. The rotor state vector is

$$\begin{aligned}\boldsymbol{x}_{\mathrm{R}}^T = [&\beta_0\ \beta_{1c}\ \beta_{1s}\ \beta_{0D}\ \dot{\beta}_0\ \dot{\beta}_{1c}\ \dot{\beta}_{1s}\ \dot{\beta}_{0D}\ \zeta_0\ \zeta_{1c}\ \zeta_{1s}\ \zeta_{0D}\\ &\dot{\zeta}_0\ \dot{\zeta}_{1c}\ \dot{\zeta}_{1s}\ \dot{\zeta}_{0D}\ \lambda_0\ \lambda_{1c}\ \lambda_{1s}\ \psi]\end{aligned} \tag{20}$$

where $\beta_0,\ \beta_{1c},\ \beta_{1s},\ \beta_{0D}$ are the flapping angles in multi-blade coordinates, $\zeta_0,\ \zeta_{1c},\ \zeta_{1s},\ \zeta_{0D}$ are the lead–lag angles in multiblade coordinates, $\lambda_0,\ \lambda_{1c},\ \lambda_{1s}$, are the main rotor induced inflow ratio harmonics, and ψ is the azimuth angle of a reference blade. Note that when the rotor is two-way coupled with the free-vortex wake, the Pitt–Peters inflow states are bypassed and the induced velocities at each blade element as predicted by the free-vortex wake are used instead. The rotor control input vector is

$$\boldsymbol{u}_{\mathrm{R}}^T = [\theta_{1c}\ \theta_{1s}\ \theta_0\ u\ v\ w\ p\ q\ r\ \dot{u}\ \dot{v}\ \dot{w}\ \dot{p}\ \dot{q}\ \dot{r}\ \Omega\ \dot{\Omega}] \tag{21}$$

where $\theta_{1c},\ \theta_{1s},\ \theta_0$ are lateral and longitudinal cyclic, and collective rotor inputs, $u,\ v,\ w$ are the longitudinal, lateral, and vertical velocities in the body-fixed frame, $p,\ q,\ r$ are the roll, pitch, and yaw rates in the body-fixed frame, and Ω and $\dot{\Omega}$ are, respectively, the main rotor angular speed and acceleration.

Note that u, v, w, p, q, r are the states of the rigid-body (or fuselage) dynamics. However, because the fuselage dynamics is not included in this study, these variables are treated as inputs to the rotor module. No powerplant dynamics is included either, such that the angular speed and acceleration of the rotor are control inputs as well.

Flapping wing kinematics and aerodynamics

Consider the wing kinematics of a flapping-wing vehicle at hover as shown in Fig. 2. A triangular waveform is used for the flapping motion for simplicity:

$$\phi(t) = \begin{cases}\Phi_0 + \frac{4\Phi}{T}\left(t - \frac{T}{4}\right) & 0 \le t < \frac{T}{2}\\ \Phi_0 - \frac{4\Phi}{T}\left(t - \frac{3T}{4}\right) & \frac{T}{2} \le t < T\end{cases} \tag{22}$$

where Φ_0 is an offset angle and Φ is the amplitude of the flapping motion. The wing pitching motion is assumed piecewise constant and is given by

$$\eta(t) = \begin{cases}\alpha_d & 0 \le t < \frac{T}{2}\\ \pi - \alpha_u & \frac{T}{2} \le t < T\end{cases} \tag{23}$$

where α_d and α_u are, respectively, the downstroke and upstroke angles of attack. In general, these two moments generated over the downstroke and upstroke are different and will generate a net pitching moment if there is an offset between the center of gravity (CG) and the hinge line of the wings (*i.e.*, $x_h \neq 0$). In this preliminary study, it is assumed that $x_h = 0$ and $\alpha_d = \alpha_u = \alpha_m$ (*i.e.*, symmetric pitching motion). As a result, the pitching moment necessary for equilibrium will be generated by other mechanisms. For instance, setting $\Phi_0 \neq 0$ introduces an asymmetric flapping motion such that an offset, typically known as wing bias, is created between the wing center of pressure averaged over one period and the CG, thus generating a pitching moment (Refs. 41–43). As such, Φ_0 is used to introduce a change in pitching attitude or horizontal velocity of the FWMAV, analogously to cyclic pitch in a helicopter rotor. A similar analogy can be made between the flapping amplitude Φ and the collective pitch of a helicopter, which are both used to control the heave motion (Ref. 44). The periodic equilibrium of the FWMAV both at hover and in translational motion can, therefore, be found by determining suitable values for Φ_0 and Φ.

A wing element model is used to calculate the time-varying aerodynamic coefficients of the wings. At each time step, the velocity induced by the free-vortex wake is calculated at any given wing cross-sectional element. The components of the induced velocity, $v_{i_x}(r)$, $v_{i_y}(r)$, and $v_{i_z}(r)$, where $r \in [0,\ R]$ is the spanwise coordinate of the wing, are subsequently used to compute the tangential and perpendicular velocities at each spanwise wing element section:

$$u_T(r) = \frac{4\Phi}{T}(\dot{\phi}) - v_{i_x}(r)\cos\phi + s v_{i_y}(r)\sin\phi \tag{24a}$$

$$u_P(r) = v_{i_z}(r) \tag{24b}$$

where

$$s = \begin{cases}1 & \text{Right Wing}\\ -1 & \text{Left Wing}\end{cases} \tag{25}$$

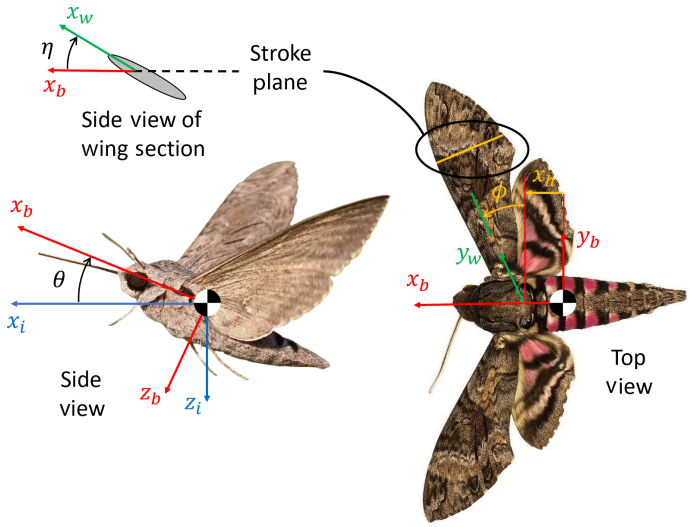

Fig. 2. Schematic diagram of a hovering FWMAV (recreated from Ref. 48).

The angle of attack of each blade element is given by

$$\alpha(r) = \alpha_m - \tan^{-1}\left(\frac{u_P}{|u_T|}\right) \tag{26}$$

The lift distribution on the wing can be then found as

$$L(r) = \tfrac{1}{4}\rho\left[u_T^2(r) + u_P^2(r)\right]c(r)ra_0\sin\left(2\alpha(r)\right) \tag{27}$$

where $c(r)$ is the chord of each wing element, a_0 is the sectional lift curve slope, and ρ is the air density. The chord distribution is calculated using the following equation from Ref. 45:

$$c(r) = B_i\bar{c}r^{c_1}(1-r)^{c_2} \tag{28}$$

where B_i is the e ratio of the maximum nondimensional chord length for the actual insect wing to the maximum nondimensional chord length and c_1 and c_2 are coefficients unique to the insect in consideration. The bound circulation at the wing element is then found based on the lift distribution:

$$\Gamma_B(r) = \frac{L(y)}{\rho\sqrt{u_T^2(r) + u_P^2(r)}} \tag{29}$$

Finally, the circulation strength of the tip vortex is taken to be the maximum value of the bound circulation of the wing (Refs. 46, 47):

$$\Gamma = \text{sign}(\dot{\phi})\max\left[\Gamma_B(r)\right] \tag{30}$$

Note that the sign of the circulation changes with upstroke/downstroke and with the wing in consideration. The parameters used in this study are representative of a hawk moth and are taken from Refs. 20 and 45. These parameters are provided in Table 1. Because prescribed wing kinematics are assumed in this work, no dynamics, and thus no states, are associated with the wing motion. As a result, the state vector of the wing dynamics is null.

State-Space Free-Vortex Wake

Rotary-wing version

A state-space free-vortex wake model is implemented into the PSUHeloSim flight simulation code following the model of Refs. 17 and 18.

Table 1. Longitudinal dynamics parameters of an FWMAV representative of a hawk moth (Refs. 6, 45)

Parameter	Numerical Value	Units
R	5.19×10^{-4}	m
$\bar{c}$	1.83×10^{-4}	m
a_0	2π	1/rad
m	1.648×10^{-6}	kg
g	9.80665	m/s^2
r_h	0	m
Ω	165.2478	rad/s
α_m	26.75	deg
B_i	1.7462	–
p	0.125	–
q	0.5	–

In PDE form, trajectory of a wake node at nondimensional time ψ and wake age ζ is governed by

$$\frac{\partial \boldsymbol{r}(\psi,\zeta)}{\partial\psi} + \frac{\partial \boldsymbol{r}(\psi,\zeta)}{\partial\zeta} = \frac{1}{\Omega}\boldsymbol{V}\left(\boldsymbol{r}(\psi,\zeta)\right) \tag{31}$$

where the right-hand side is governed by the Biot–Savart law, which is the most expensive part of the free-wake computation. The wake model was implemented in state-variable form generally following the approach of Ref. 16, with some updates. Specifically, the model includes states to define vortex strength at each of the free wake nodes, allowing for varying vortex strength along the filament. The model assumes linearly varying vortex strength along each linear vortex line segment, following the formulation of Ref. 49. The vortex strength state of the youngest node is defined as the peak circulation on the blade from which filament originates. This same vortex strength then propagates along the filament as the age of the segment increases. Assuming vortex strength is conserved, the PDE representation is simply

$$\frac{\partial\Gamma(\psi,\zeta)}{\partial\psi} + \frac{\partial\Gamma(\psi,\zeta)}{\partial\zeta} = 0 \tag{32}$$

This expression can then be converted to first-order ordinary differential equations (ODE) from using the same approach as in Ref. 16. Age-dependent terms can also be added to account for decay and core growth (although not currently featured in this preliminary implementation). In practice, to avoid algebraic loop due to the feedback of the induced velocities at the rotor blades, $\boldsymbol{v}_i$, the induced velocities at the rotor blades are added to the system of ODE as states. Their dynamics are governed by a first-order filter with a time constant of $\tau_{\boldsymbol{v}_i} = 0.005$ s. The resulting system of ODE expressed in dimensional time is:

$$\dot{\boldsymbol{r}} = -\Omega\boldsymbol{A}_\zeta\boldsymbol{r} + \boldsymbol{V}\left(\boldsymbol{r}(t,\zeta)\right) \tag{33a}$$

$$\dot{\boldsymbol{\Gamma}} = -\Omega\boldsymbol{A}_\zeta\boldsymbol{\Gamma} \tag{33b}$$

$$\dot{\boldsymbol{v}}_i = \frac{1}{\tau_{\boldsymbol{v}_i}}\left[\boldsymbol{V}\left(\boldsymbol{r}_B(t,\zeta)\right) - \boldsymbol{v}_i\right] \tag{33c}$$

where $\boldsymbol{A}_\zeta$ is the finite difference matrix corresponding to the 5PBU4 scheme from Ref. 16 and $\boldsymbol{r}_B$ is the position of the rotor blade elements.

As such, the coupled rotor and free-vortex wake dynamics is formulated as an NLTP system in the first-order form:

$$\dot{\boldsymbol{x}} = \boldsymbol{f}(\boldsymbol{x},\boldsymbol{u},t) \tag{34a}$$

$$\boldsymbol{y} = \boldsymbol{g}(\boldsymbol{x},\boldsymbol{u},t) \tag{34b}$$

where $\boldsymbol{x} \in \mathbb{R}^n$ is the state vector, $\boldsymbol{u} \in \mathbb{R}^m$ is the control input vector, $\boldsymbol{y} \in \mathbb{R}^l$ is the output vector, and t is the dimensional time in seconds.

The nonlinear functions $\boldsymbol{f}$ and $\boldsymbol{g}$ are T-periodic in t such that

$$\boldsymbol{f}(\boldsymbol{x},\boldsymbol{u},t) = \boldsymbol{f}(\boldsymbol{x},\boldsymbol{u},t+T) \tag{35a}$$

$$\boldsymbol{g}(\boldsymbol{x},\boldsymbol{u},t) = \boldsymbol{g}(\boldsymbol{x},\boldsymbol{u},t+T) \tag{35b}$$

It is convenient to note that dimensional time can be related to the azimuth angle ψ of a reference blade, also known as nondimensional time, via the following relation: $\psi = \Omega t$, where Ω the main rotor angular speed in rad/s. It follows that the fundamental period of the system is $T = \frac{2\pi}{\Omega}$ seconds, which corresponds to 2π radians or one rotor revolution. The state vector is constituted by the rotor states and the free-wake states such that $\boldsymbol{x}^T = [\boldsymbol{x}_\mathrm{R}^T\ \boldsymbol{x}_\mathrm{W}^T]$, where $\boldsymbol{x}_\mathrm{R}$ is the rotor state vector and $\boldsymbol{x}_\mathrm{W}^T = [\boldsymbol{r}^T\ \boldsymbol{\Gamma}^T\ \boldsymbol{v}_i^T]$ is the rotor wake state vector. The control input vector is assumed equal to the rotor control input vector such that $\boldsymbol{u} = \boldsymbol{u}_\mathrm{R}$. The output vector comprises the state vector, the induced velocities at the blade elements, and the rotor forces and moments such that $\boldsymbol{y}^T = [\boldsymbol{x}_\mathrm{R}^T\ \boldsymbol{x}_\mathrm{W}^T\ \boldsymbol{v}_i^T\ X_\mathrm{R}\ Y_\mathrm{R}\ Z_\mathrm{R}\ L_\mathrm{R}\ M_\mathrm{R}\ N_\mathrm{R}]$.

Flapping-wing version

Because in flapping-wing vehicles the flapping-wing speed may not coincide with nondimensional time|in fact, this is the case when $\Phi \neq 90$ deg|the state-space formulation needs modifications to account for this. In the PDE form, trajectory of a wake node at flapping angle ϕ and wake age ζ is governed by

$$\dot{\phi}\frac{\partial \boldsymbol{r}(\phi,\zeta)}{\partial \phi} + \Omega\frac{\partial \boldsymbol{r}(\phi,\zeta)}{\partial \zeta} = \boldsymbol{V}\left(\boldsymbol{r}(\phi,\zeta)\right) \tag{36}$$

where $\dot{\phi}$ is the wing flapping speed and Ω is the fundamental frequency of the system, both expressed in rad/s. The right-hand side is governed by the Biot–Savart law, which is the most expensive part of the free-wake computation. The flapping speed and fundamental frequency are related by $\dot{\phi} = \frac{2}{\pi}\Phi\Omega$, where Φ is the amplitude of the flapping motion. The fundamental frequency of the system is given by $\Omega = \frac{2\pi}{T}$, where T is the period of a full wing beat. The wake model was implemented in state-variable form generally following the approach of Ref. 16, with significant updates. By applying the same approach as before, and as in Ref. 16, the resulting system of ODE expressed in dimensional time is

$$\dot{\boldsymbol{r}} = -\frac{\Omega}{\dot{\phi}}\boldsymbol{A}_\zeta \boldsymbol{r} + \frac{1}{\dot{\phi}}\boldsymbol{V}\left(\boldsymbol{r}(t,\zeta)\right) \tag{37a}$$

$$\dot{\boldsymbol{\Gamma}} = -\frac{\Omega}{\dot{\phi}}\boldsymbol{A}_\zeta \boldsymbol{\Gamma} \tag{37b}$$

$$\dot{\boldsymbol{v}}_i = \frac{1}{\tau_{v_i}}[\boldsymbol{V}(\boldsymbol{r}_\mathrm{B}(t,\zeta)) - \boldsymbol{v}_i] \tag{37c}$$

where $\boldsymbol{A}_\zeta$ is the finite difference matrix corresponding to the 5PBU4 scheme from Ref. 16 and $\boldsymbol{r}_\mathrm{B}$ is the position of the wing elements. A static viscous core decay model is implemented based on Refs. 50 and 51, where the vortex core radius is a function of wake age

$$r_c(\zeta) = \sqrt{r_{c_0} + \frac{4\alpha\delta\nu\zeta}{\Omega}} \tag{38}$$

where ν is the air viscosity, $\alpha = 1.25643$, and $\delta = 1$. Additionally, $r_{c_0} = 0.25\bar{c}$ as suggested in Ref. 52.

As such, the free-vortex wake dynamics is formulated as an NLTP system in the first-order form like that in Eq. (34). The fundamental period in this case corresponds to 2π radians or one wing beat. The state vector is constituted by free-wake states such that

$$\boldsymbol{x}^T = \left[\boldsymbol{r}^T\ \boldsymbol{\Gamma}^T\ \boldsymbol{v}_i^T\right] \tag{39}$$

is the wake state vector. The control input vector $\boldsymbol{u}$ includes the amplitude of the flapping motion and the wing bias such that $\boldsymbol{u}^T = [\Phi\ \Phi_0]$. The output vector comprises the state vector and the induced velocities at the wing elements such that $\boldsymbol{y}^T = [\boldsymbol{x}^T\ \boldsymbol{v}_i^T]$. Because the wake model is effectively expressed as an NLTP system, periodic solutions, and approximate higher order LTI models can be found with the modified harmonic balance method of Ref. 36. With the method described above, the approach in Ref. 16 is effectively extended from rotary-wing applications to flapping-wing flight. This constitutes one of the major novelties introduced by this article.

Results

Rotary-wing vehicle

Implementation and validation. The coupled rotor and state-space free-vortex wake model is implemented in MATLAB®/Simulink using a 10-deg time step and three revolutions of rotor wake. The resulting NLTP system has a state vector with dimension $n = 1872$ (20 rotor states and 1852 wake states), a control vector with dimension $m = 17$, and an output vector of dimension $l = 1918$. Figure 3(a) shows a representation of a computed wake at an advance ratio of 0.1. Note that the wake position states are inherently periodic (*e.g.*, in equilibrium the lateral position of a wake node of a certain age oscillates at 1/rev, with amplitude equal to the width of the wake at that location). Figure 3(b) shows the position for a wake state in the simulation shown previously, with four different wake ages 270 deg apart. The 1/rev oscillation and expected phasing are clearly seen, with higher harmonic distortions increasing as the wake ages. These kinds of waveforms are readily approximated by a truncated Fourier series. This allows the periodic wake dynamics to be approximated as time invariant through the harmonic decomposition method.

Linearized models. A first step towards the linearization of the system involves solving for the periodic equilibrium $x^*(t)$ and $u^*(t)$. Because both the rotor and wake dynamics are stable, such that the coupled system is stable, the periodic equilibrium is found by time marching the system until it reaches its periodic equilibrium. The initial rotor states and control inputs are found by trimming the coupled fuselage (not included in this study) and rotor dynamics without free wake at a 0.1 advance ratio. This was done to have control inputs representative of the full vehicle trim for the flight condition in consideration. The control inputs are then frozen, and the coupled rotor and wake dynamics are time-marched until convergence. In practice, this requires approximately four rotor revolutions. Then, the system is linearized about the periodic equilibrium thus found at incremental time steps over one rotor revolution to yield a set of LTI systems that together constitute an LTP system. In a subsequent step, harmonic decomposition is applied to approximate the LTP system with a higher order LTI model by retaining up to the fourth state and output harmonics (*i.e.*, $N = L = 4$). Only the zeroth harmonic of the input is retained as this study only considers control inputs with a frequency considerably lower than the rotor angular speed (*i.e.*, $M = 0$). This translates into being able to only predict the influence of low-frequency control inputs (*i.e.*, primary flight controls) on the averaged and higher harmonic content of the response. Note that one would have to retain control input harmonics higher than the zeroth (*i.e.*, $M > 0$) in the case of higher harmonic control . The resulting LTI system has 16,848 states, 17 control inputs, and 17,262 outputs. The eigenvalues of the high-order, residualized, and averaged dynamics are shown in Fig. 4. Notably, all eigenvalues of the high-order LTI model are strictly negative, such that the use of residualization is justified.

To assess the accuracy of the harmonic decomposition model thus obtained, the response of the high-order LTI dynamics is compared to

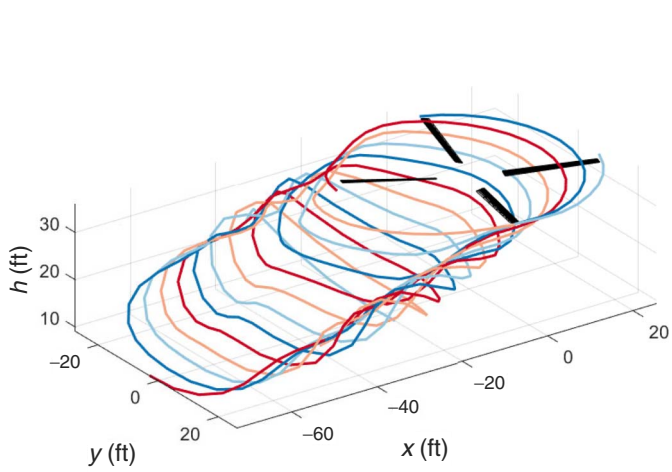

(a) Three-dimensional visualization of the free-vortex wake

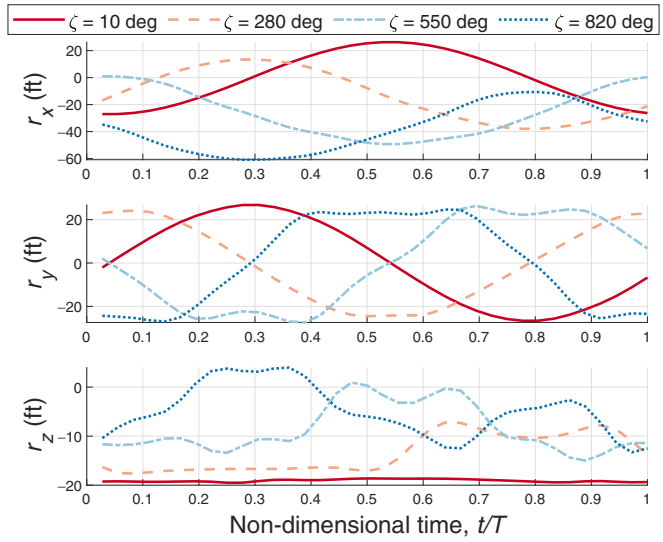

(b) Representative wake node locations in periodic equilibrium

Fig. 3. State-space free-vortex wake integrated with a blade element model of the UH-60 rotor.

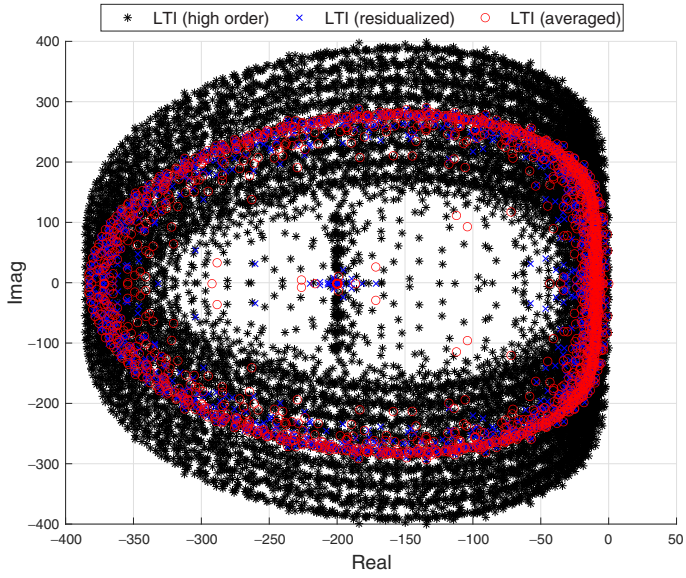

Fig. 4. Eigenvalues of the coupled rotor and wake dynamics.

that of the nonlinear dynamics. Figure 11 shows some responses of the nonlinear, high-order LTI, and averaged LTI dynamics to a 3-deg doublet in the collective control input. Figure 5(a) shows the perturbation of one of the wake vortex nodes from the periodic equilibrium. In this figure, the response of the harmonic decomposition model (high-order LTI model) nearly overlaps the response of the nonlinear system, indicating the validity of the proposed method. On the other hand, as expected, the averaged LTI dynamics is not able to capture the oscillatory behavior of the rotor wake states. This figure also shows the response of the residualized LTI model. The model was obtained by residualizing the states corresponding to the higher harmonics while retaining all state harmonics as part of the output. Note that each output perturbation response from this model is reconstructed from that output harmonic coefficients time history using Eq. (8c). Likewise, each state perturbation response from the high-order LTI model is reconstructed from that state harmonic coefficient time history using Eq. (8a). Although the residualized model is the same order as the averaged dynamics, it is capable of predicting the higher harmonic content, nearly overlapping both high-order LTI and NLTP model responses. In Fig. 5(b), the induced velocity at one of the blade elements (approximately located at 76% radius) is shown. The high-order LTI model better captures the oscillatory velocity profile of the nonlinear model compared to the averaged LTI model. Indeed, the averaged model is not expected to capture any peaks; it just captures the averaged response, not the oscillations. The residulized model gives a very similar response to the high-order LTI model.

Similar trends are observed in Fig. 6. This figure shows the contour plot of induced velocities over one revolution at different sample time periods for the response to a 3-deg doublet in collective pitch described above. The left column shows the inflow contours during the initial periodic equilibrium. The results show the expected longitudinal inflow gradient in forward flight trim, and the contours are nearly identical for all models. This is expected since the periodic equilibrium from the nonlinear model is superimposed on the perturbation solution of the linear model, and at that stage there are no perturbations from equilibrium. The next two columns show contours for rotor revolutions shortly after the positive collective input and the negative collective steps, respectively. The expected increase and then reduction in inflow velocities are seen for all models. However, the averaged LTI model significantly underpredicts the positive inflow perturbation, notably on the aft retreating quadrant of the rotor. The high-order and reduced-order LTI models do a better job of capturing the inflow distribution for the positive collective step. However, the LTI models do have some characteristic differences compared with the NLTP model. The NLTP model seems to indicate that there is more left/right symmetry in induced inflow (Fig. 6(b)) compared to the LTI models where the advancing side generates more induced inflow (Figs. 6(e) and 6(h)). This may indicate that there is roll-due-to-collective coupling in the LTI models that is stronger compared to the NLTP model. This is further substantiated by the roll moment response shown in Fig. 7. The contours after the negative collective step show a reasonable correlation, although the LTI models show more distortion in the inflow on the front retreating quadrant.

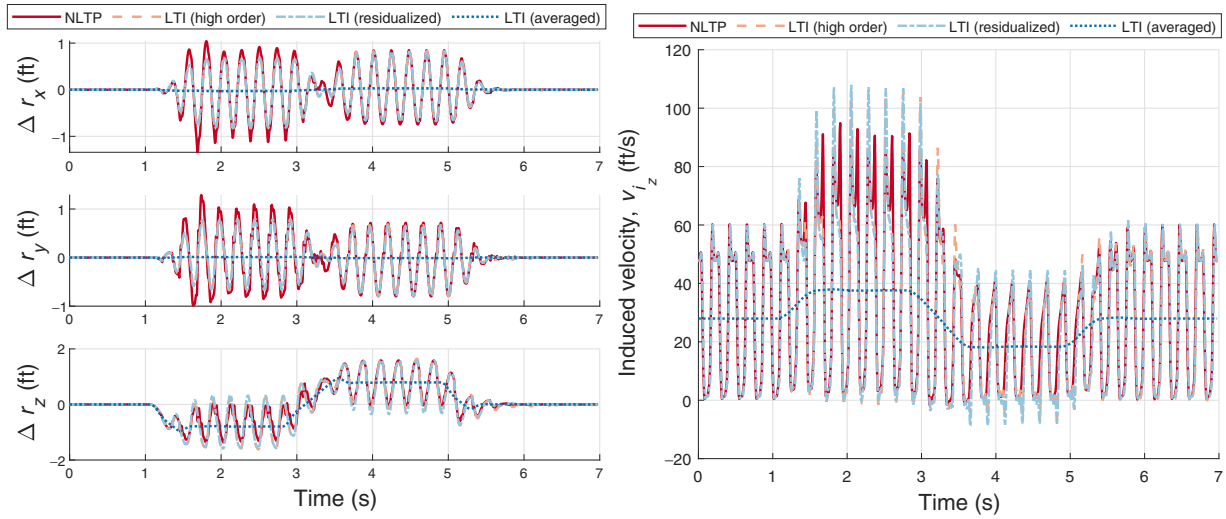

(a) Sample wake node position (perturbation from periodic equilibrium)

(b) Induced velocity at blade element at 76% rotor radius

Fig. 5. Time history of some periodic states following a 3-deg doublet in collective pitch.

Runtime performance. The runtime performance is assessed for each of the simulation models and compared. Using a MATLAB® R2022a implementation and the fourth-order Runge–Kutta solver on a 2021 MacBook Pro computer equipped with an Apple M1 Max processor, simulation of the NLTP model runs approximately 89× slower than real-time. The high-order LTI model reduces slightly the runtime to 76× slower than real-time. On the other hand, the residualized LTI model runs 1.4× slower than real-time while providing very similar predictions to those of the NLTP and high-order LTI models. This is approximately a 64× runtime improvement with respect to the NLTP simulation. It is speculated that by increasing the simulation time step, by further reducing the order of the system, and/or by performing the simulation on a faster machine, real-time prediction simulation may be possible. It is also worth noting these models are available in Simulink and could be autocoded to C for faster executions. Lastly, the averaged dynamics of the coupled rotor and vortex wake runs approximately 1.6× faster than real-time. However, it does not retain information on the higher harmonics of the system. These results are reported in Table 2, along with the time associated with the computation of a time step for each simulation strategy.

Flapping-wing vehicle

Implementation and validation. The state-space free-vortex wake model is integrated with the flapping-wing model described above and tested for hover conditions and simple control inputs. Note that the triangular waveform gives piecewise constant flapping speed (*i.e.*, $|\dot{\phi}| = \text{const.}$). The model is implemented in MATLAB®/Simulink using a 10-deg time step and three wing beat cycles of wake. The resulting NLTP system has a state vector with dimension $n = 924$ (all of which wake states), a control vector with dimension $m = 2$, and an output vector of dimension $l = 944$. Figure 8 shows a representation of the wake computed at hover. In this figure, the state-space free-vortex wake is shown to capture important aerodynamic phenomena related to flapping-wing flight and that are found in the literature (see, *e.g.*, Refs. 9, 13, 53, 54), which are described as follows. First, it is clear that the reciprocating wing flapping motion, combined with the inducted flow through the wing, creates a series of folded surfaces of trailed vorticity. Layers (sheets) of vorticity of opposing sign that are convected below, and roughly parallel to, the stroke plane (Fig. 8(b)). Second, a large flow recirculation region is generated in the plane of flapping and centered around the wing tips (Fig. 8(a)). Third, recirculation of the flow is also visible where the vortex sheets merge and roll up into more concentrated regions of vorticity (Fig. 8(b)). Fourth, the wake appears to contract below the stroke plane because of the acceleration of the air (Fig. 8(a)), in accordance with momentum theory (Ref. 45). The induced velocity at the stroke plane is in line with those observed in the literature. However, as expected, the model does not capture the typical leading-edge vortex originating from the separated flow on the outboard regions of the wing (Ref. 53). This is because the current free-wake model assumes that the entire circulation of the wing is convected into a single tip vortex. Note that the wake position states are inherently periodic (*e.g.*, in equilibrium the lateral position of a wake node of a certain age oscillates with amplitude equal to the width of the wake at that location). Figure 9 shows the position for a wake state in the simulation shown previously, with four different wake ages 270 deg apart. The one-per-cycle (*i.e.*, 1/cycle) and 2/cycle oscillations and expected

Table 2. Runtime performance with a time step of $\Delta\psi = \Delta\zeta = 10$ deg and three rotor wake revolutions

Simulation Type	1 Time Step (s)	× Real Time	Number of States	Number of Outputs
NLTP	5.8e−1	89	1,872	1,918
High-order LTI	4.9e−1	76	16,848	17,262
Residualized LTI	9.3e−3	1.4	1,872	17,262
Averaged LTI	3.9e−3	0.6	1,872	1,918

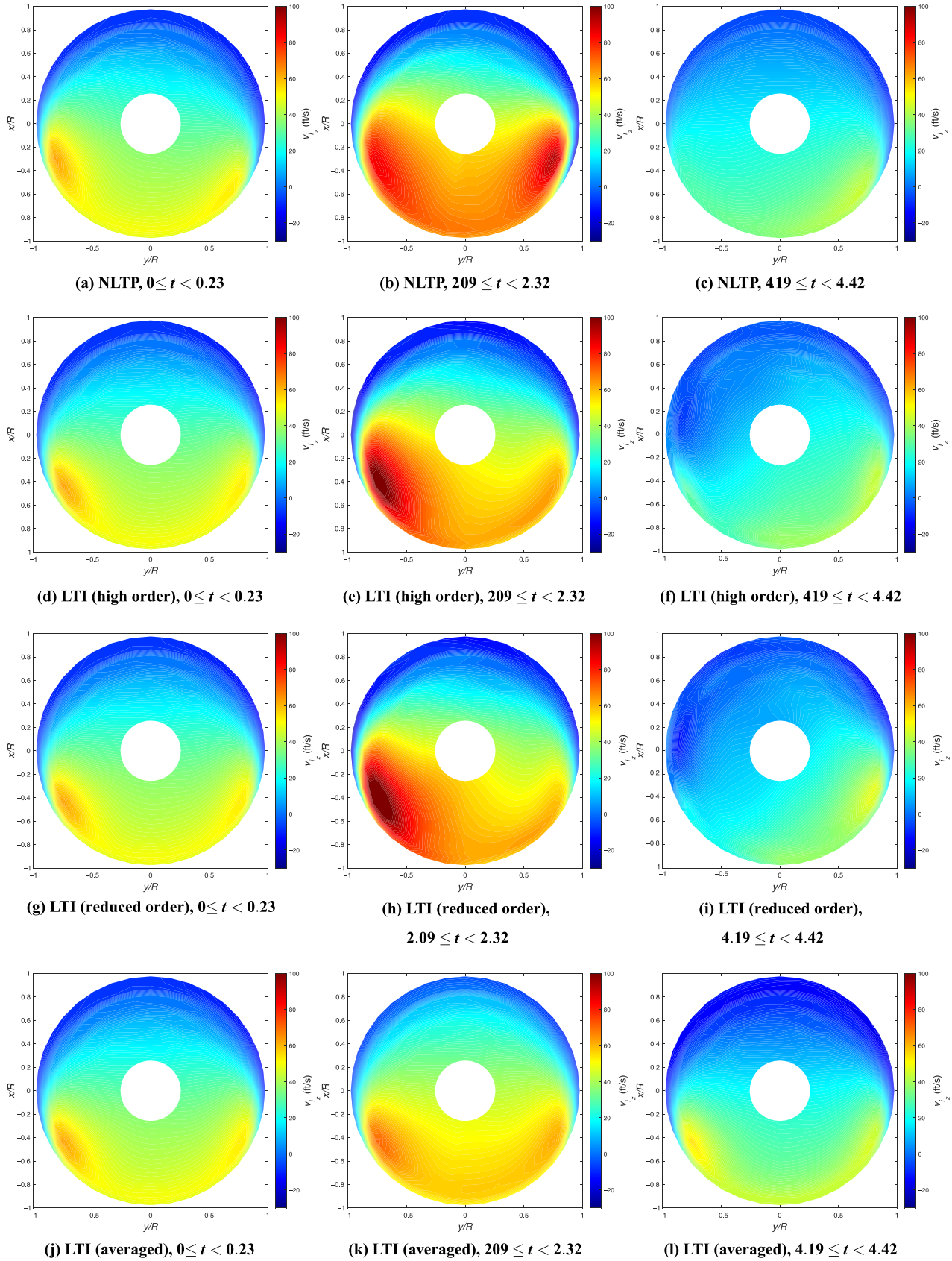

(a) NLTP, $0 \leq t < 0.23$ (b) NLTP, $209 \leq t < 2.32$ (c) NLTP, $419 \leq t < 4.42$

(d) LTI (high order), $0 \leq t < 0.23$ (e) LTI (high order), $209 \leq t < 2.32$ (f) LTI (high order), $419 \leq t < 4.42$

(g) LTI (reduced order), $0 \leq t < 0.23$ (h) LTI (reduced order), $2.09 \leq t < 2.32$ (i) LTI (reduced order), $4.19 \leq t < 4.42$

(j) LTI (averaged), $0 \leq t < 0.23$ (k) LTI (averaged), $209 \leq t < 2.32$ (l) LTI (averaged), $4.19 \leq t < 4.42$

Fig. 6. Contour plot of induced velocities over one revolution at different sample time periods following a 3-deg doublet in collective pitch. Free-stream air velocity is moving from top to bottom; advancing side is $y/R > 0$, retreating side is $y/R < 0$.

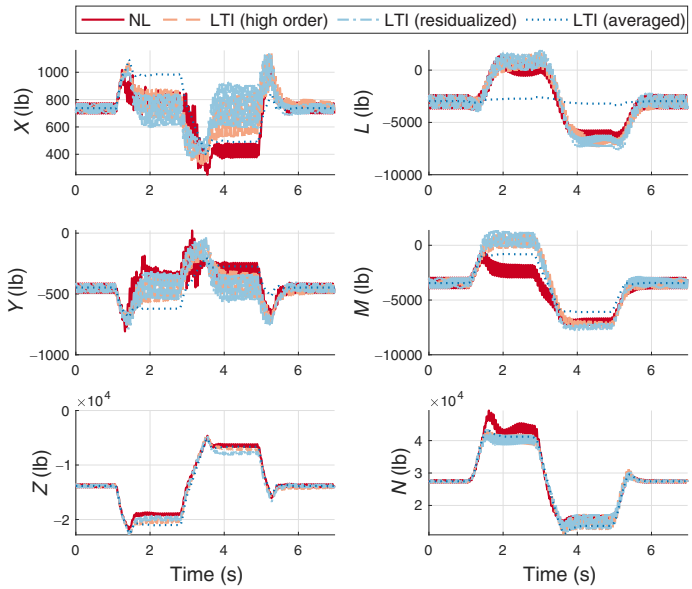

Fig. 7. Rotor forces and moments response to a 3-deg doublet in collective pitch.

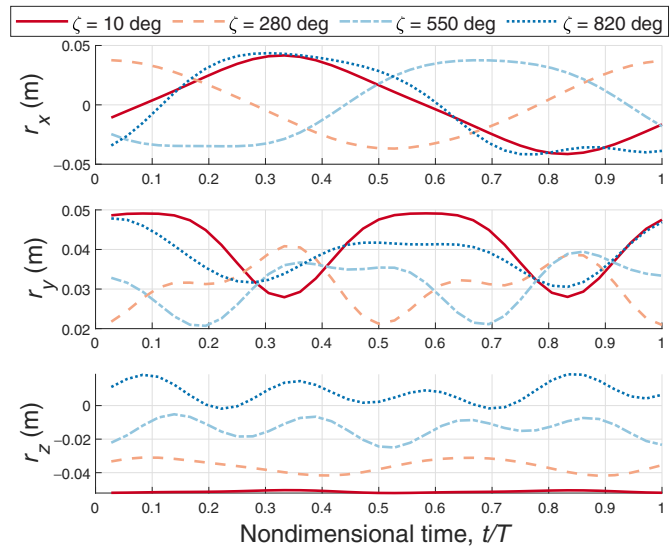

Fig. 9. Vortex node position over a single wing beat and for varying wake age.

phasing is clearly seen, with higher harmonic distortions increasing as the wake ages. These kinds of waveforms are readily approximated by a truncated Fourier series. This allows the periodic wake dynamics to be approximated as time invariant through the harmonic decomposition method (Refs. 28, 29).

Linearized models. A first step towards the linearization of the system involves solving for the periodic equilibrium $x^*(t)$ and $u^*(t)$. Because the wake dynamics may be unstable, time marching the wake dynamics may not result in a convergence to the periodic equilibrium. As such, the modified harmonic balance of Ref. 36 is used to solve for the periodic equilibrium. Then, the system is linearized about the periodic equilibrium thus found at incremental time steps over one wing beat to yield a set of LTI systems that together constitute an LTP system. In a subsequent step, harmonic decomposition is applied to approximate the LTP system with a higher order LTI model by retaining up to the fourth state and output harmonics (*i.e.*, $N = L = 4$). Only the zeroth harmonic of the input is retained as this study only considers control inputs with frequency considerably lower than the fundamental frequency (*i.e.*, $M = 0$). This translates into being able to only predict the influence of low-frequency control inputs on the averaged and higher harmonic content of the response. The resulting LTI system has a total of 8316 states, two control inputs, and 8496 outputs. The eigenvalues of the high-order, residualized, and averaged dynamics are shown in Fig. 10. Notably, a relatively low number of eigenvalues of the high-order LTI model lies in the right-hand side of the complex plane, but close to the origin. This violates the assumptions of residualization. It is not clear whether this is a numerical instability or an instability related to the physics of the wake. Because the number of eigenvalues is very low compared to the order of the system, and because these eigenvalues are close to the imaginary axis, residualization is still applied to the high-order LTI model. The eigenvalues of the residualized dynamics are also shown in Fig. 10 and show a similar qualitative distribution to those of the coupled rotor and wake dynamics analyzed earlier (Fig. 4). In any case, other order-reduction methods should be considered in the future that do not require asymptotical stability.

To assess the accuracy of the harmonic decomposition model thus obtained, the response of the high-order LTI dynamics is compared to that of the nonlinear dynamics. Figure 11 shows some responses of the nonlinear, high-order LTI, and averaged LTI dynamics to a 10-deg doublet in the flapping motion amplitude Φ. Figure 11(a) shows the perturbation of one of the wake vortex nodes from the periodic equilibrium. In this figure, the response of the harmonic decomposition model (high-order

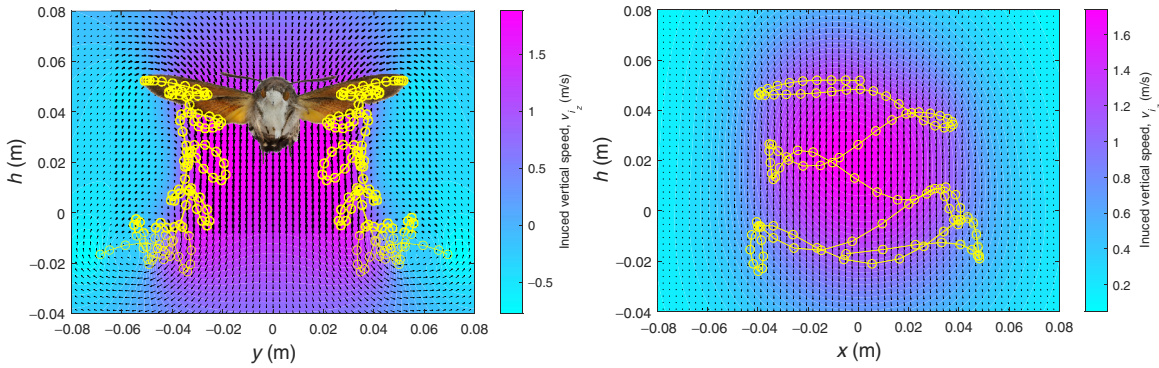

(a) Frontal visualization of the state-space free-vortex wake **(b) Lateral visualization of the state-space free-vortex wake**

Fig. 8. State-space free-vortex wake model as applied to a hawk moth.

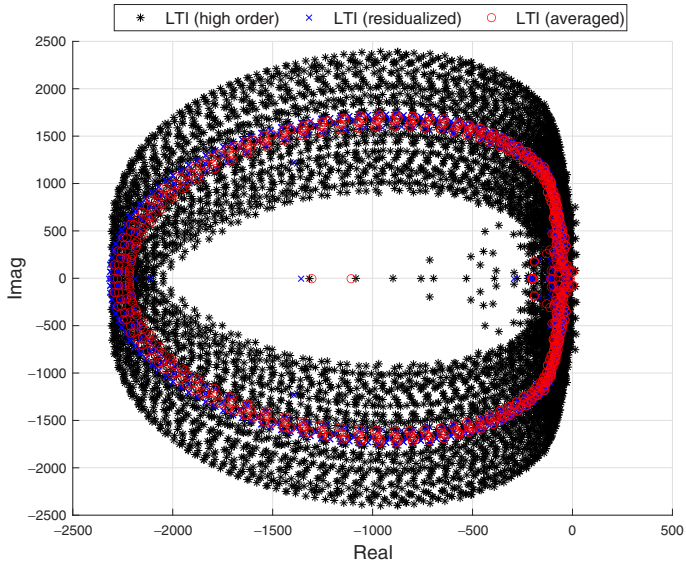

Fig. 10. Eigenvalues of the flapping-wing wake dynamics.

LTI model) nearly overlaps the response of the nonlinear system, indicating the validity of the proposed method. On the other hand, as expected, the averaged LTI dynamics does not capture the oscillatory behavior of the wake states. In Fig. 11(b), the induced velocity at one of the blade elements (approximately located at 76% radius) is shown. Note that each output response from this model is reconstructed from that output harmonic coefficients time history using Eq. (8c). Although the residualized model is the same order as the averaged dynamics, the residualized model is capable of predicting the higher harmonic content, nearly overlapping both high-order LTI and NLTP model responses. The averaged LTI model only predicts the average behavior of the response. It is concluded that it is possible to derive linearized harmonic decomposition models of the free-vortex wake that provide accurate predictions of the nonlinear wake dynamics.

Runtime performance. The runtime performance is assessed for each of the simulation models and compared using the same computer and integration scheme as in the previous example. Based on this setup, simulations of the NLTP model run approximately 144 times slower than real time. The high-order LTI model increased the runtime to 211 times slower than real time. On the other hand, the residualized LTI model runs three times slower than real-time while providing very similar predictions to those of the NLTP and high-order LTI models. This is approximately a 48× runtime improvement with respect to the NLTP simulation. It is speculated that by reducing the simulation time step, by further reducing the order of the system via, for instance, balanced realization, and/or by performing the simulation on a faster machine, real-time prediction simulation may indeed be possible. Lastly, the averaged dynamics of the free-vortex wake runs approximately 1.4 times slower than real-time. However, it does not retain information on the higher harmonics of the system. These results are reported in Table 3, along with the time associated with the computation of a time step for each simulation strategy.

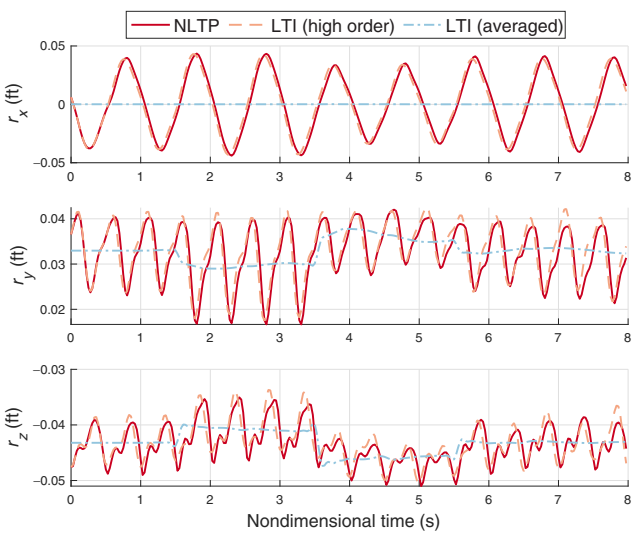

(a) Sample wake node position at wake age $\zeta = 180$ deg

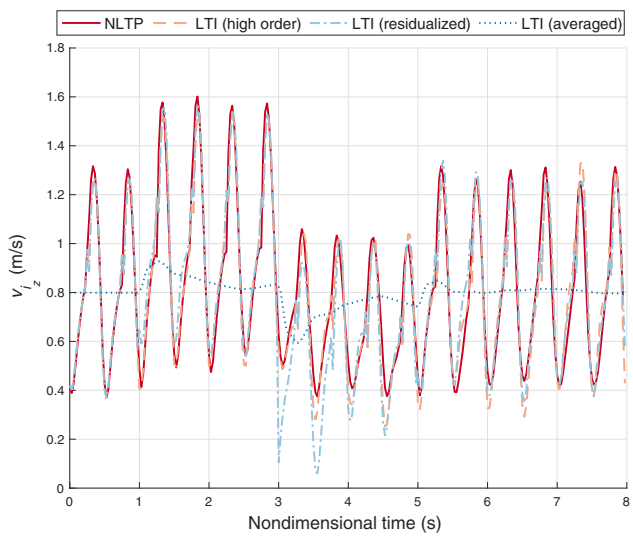

(b) Induced velocity at wing element at 75% wing span

Fig. 11. Time history of some periodic states following a 10-deg doublet in the flapping motion amplitude.

Table 3. Runtime performance with a 10-deg time step and three wing beat cycles of wake

Simulation Type	1 Time Step (s)	× Real Time	Number of States	Number of Outputs
NLTP	1.5e−1	144	924	944
High-order LTI	2.0e−1	211	8316	8496
Residualized LTI	3.1e−3	3	924	8496
Averaged LTI	1.4e−3	1.4	924	944

Conclusions

This article describes the implementation and linearization of free-vortex wake models in state-variable form as applied to rotary- and flapping-wing vehicles. Free-vortex wake models were implemented and tested for a UH-60 rotor in forward flight and for a hovering insect representative of a hawk moth. A periodic solution to each wake model was found by time marching the coupled rotor/wing and vortex wake dynamics. Next, linearized harmonic decomposition models were obtained and validated against nonlinear simulations. Order reduction methods were explored to guide the development of linearized wake models that provide increased runtime performance compared to the nonlinear and linearized harmonic decomposition wake models while guaranteeing satisfactory prediction of the periodic response of the wake. To the best knowledge of the authors, this effort constituted a very first attempt to extend free-vortex wake methods in state-variable form, originally developed for rotary-wing applications, to flapping-wing flight. Based on the current work, the following conclusions can be reached:

1) The free-vortex wake model in state variable form originally proposed for rotary-wing applications is qualitatively shown to capture important aerodynamic phenomena related to flapping-wing flight. More definitive conclusions will require a quantitative validation against results in the literature. Modifications to the model were necessary to account for the difference between wing flapping speed and fundamental frequency of the system. In rotary-wing vehicles, where the flapping motion of the wing is equivalent to the blade angular speed, blade angular speed and fundamental frequency of the system are equal.

2) Linearized harmonic decomposition models are shown to predict accurately the nonlinear wake response for the cases shown and for relatively small amplitude control inputs. More study is required to understand over what amplitude range the linear models will be accurate. While these harmonic decomposition models do not necessarily result in increased runtime performance when compared to the nonlinear dynamics, their order can be conveniently reduced with LTI model-order reduction methods.

3) Reduced-order models obtained by residualizing the linearized harmonic decomposition models are shown to provide an accurate prediction of the nonlinear wake dynamics at a fraction of the computational cost. Notably, for the rotary-wing test case shown, runtime of these models approach real-time.

4) Averaged models provide the most reduction in simulation runtime, resulting in real-time performance for rotary-wing vehicles but do not predict the higher harmonics of the wake dynamics. In fact, these models only predict the averaged, or zeroth harmonic, response.

Acknowledgments

This research was partially funded by the U.S. Government under agreement no. W911W6-21-2-0002. The views and conclusions contained in this document are those of the authors and should not be interpreted as representing the official policies, either expressed or implied, of the Aviation Development Directorate or the U.S. Government.

References

[1]Howlett, J. J., "UH-60A Black Hawk Engineering Simulation Program. Volume 1: Mathematical Model," Technical report, NASA-CR-166309, 1980.

[2]Horn, J. F., Bridges, D. O., Wachspress, D. A., and Rani, S. L., "Implementation of a Free-Vortex Wake Model in Real-Time Simulation of Rotorcraft," *AIAA Journal of Computing, Information, and Communications*, Vol. 3, (3), March 2006, pp. 93–107, DOI: https://doi.org/10.2514/1.18273.

[3]Keller, J. D., Wachspress, D. A., and Hoffler, J. C., "Real Time Free Wake and Ship Airwake Model for Rotorcraft Flight Training Applications," Proceedings of the 71st Annual Forum of the American Helicopter Society, Virginia Beach, VA, May 5–7, 2015.

[4]Zhao, J., and He, C., "A Viscous Vortex Particle Model for Rotor Wake and Interference Analysis," *Journal of the American Helicopter Society*, **55**, 012007 (2010), DOI: https://doi.org/10.4050/JAHS.55.012007.

[5]Oruc, I., Horn, J. F., Shipman, J., and S., P., "Towards Real-Time Pilot-in-the-Loop CFD Simulations of Helicopter/Ship Dynamic Interface," *International Journal of Modeling, Simulation, and Scientific Computing*, **8**, 1743005 (2017), DOI: https://doi.org/10.1142/S179396231743005X.

[6]Taha, H. E., Hajj, M. R., and Nayfeh, A. H., "Longitudinal Flight Dynamics of Hovering MAVs/Insects," *Journal of Guidance, Control, and Dynamics*, Vol. 37, (3), 2014, pp. 970–978, DOI: https://doi.org/10.2514/1.62323.

[7]Taha, H., Hajj, M. R., and Beran, P. S., "State-Space Representation of the Unsteady Aerodynamics of Flapping Flight," *Aerospace Science and Technology*, Vol. 34, (1), 2014, pp. 1–11, DOI: https://doi.org/10.1016/j.ast.2014.01.011.

[8]Bayiz, Y. E., and Cheng, B., "State-Space Aerodynamic Model Reveals High Force Control Authority and Predictability in Flapping Flight," *Journal of The Royal Society Interface*, **18**, 20210222 (2021), DOI: https://doi.org/10.1098/rsif.2021.0222.

[9]Cheng, B., Roll, J., Liu, Y., Troolin, D. R., and Deng, X., "Three-Dimensional Vortex Wake Structure of Flapping Wings in Hovering Flight," *Journal of The Royal Society Interface*, **11**, 20130984 (2014), DOI: https://doi.org/10.1098/rsif.2013.0984.

[10]Chen, L., Wang, L., Zhou, C., Wu, J., and Cheng, B., "Effects of Reynolds Number on Leading-Edge Vortex Formation Dynamics and Stability in Revolving Wings," *Journal of Fluid Mechanics*, **931**, A13 (2022), DOI: https://doi.org/10.1017/jfm.2021.950.

[11]Chen, L., Wu, J., and Cheng, B., "Leading-Edge Vortex Formation and Transient Lift Generation on a Revolving Wing at Low Reynolds Number," *Aerospace Science and Technology*, **97**, 105589 (2020), DOI: https://doi.org/10.1016/j.ast.2019.105589.

[12]Liu, Y., Cheng, B., Barbera, G., Troolin, D. R., and Deng, X., "Volumetric Visualization of the Near- and Far-Field Wake in Flapping Wings," *Bioinspiration & Biomimetics*, **8**, 036010 (2020), DOI: https://doi.org/10.1088/1748-3182/8/3/036010.

[13]Gomez, S., Gilkey, L., Kaiser, B., and Poroseva, S., "Computational Analysis of a Tip Vortex Structure Shed from a Bio-inspired Blade," Proceedings of the 32nd AIAA Applied Aerodynamics Conference, Atlanta, GA, June 16–20, 2014, DOI: https://doi.org/10.2514/6.2014-3253.

[14]Keller, J., McKillip, R., Wachspress, D., Tischler, M., and Juhasz, O., "Linearized Inflow and Interference Models from High Fidelity Free Wake Analysis for Modern Rotorcraft Configurations," Proceedings of the 75th Annual Forum of the Vertical Flight Society, Philadelphia, PA, May 14–15, 2019.

[15]He, C., Syal, M., Tischler, M., and Juhasz, O., "State-Space Inflow Model Identification from Viscous Vortex Particle Method for Advanced Rotorcraft Configurations," Proceedings of the 73rd Annual Forum of the Vertical Flight Society, Forth Worth, TX, May 9–11, 2017.

[16]Celi, R., "State-Space Representation of Vortex Wakes by the Method of Lines," *Journal of the American Helicopter Society*, Vol. 50, (2), April 2005, pp. 195–205, DOI: https://10.4050/1.3092855.

[17]Bagai, A., and Leishman, G. J., "Rotor Free-Wake Modeling Using a Pseudo-Implicit Technique-Including Comparison with Experimental

Data," *Journal of the American Helicopter Society*, Vol. 40, (3), July 1995, pp. 29–41, DOI: https://doi.org/10.4050/JAHS.40.29.

[18]Bhagwat, M. J., *Transient Dynamics of Helicopter Rotor Wakes Using a Time-Accurate Free-Vortex Method*, Ph.D. thesis, University of Maryland, College Park, MD, 2001.

[19]Sanders, J. A., Verhulst, F., and Murdock, J., *Averaging Methods in Nonlinear Dynamical Systems*, Springer, Princeton, NJ, 2007, Chapter Averaging: the periodic case, DOI: https://doi.org/10.1007/978-0-387-48918-6.

[20]Hassan, A. M., and Taha, H. E., "Higher-Order Averaging Analysis of the Nonlinear Time-Periodic Dynamics of Hovering Insects/Flapping-Wing Micro-Air-Vehicles," Proceedings of the 55th Conference on Decision and Control, Las Vegas, NV, December 12–14, 2016, DOI: https://doi.org/10.1109/CDC.2016.7799424.

[21]Maggia, M., Eisa, S. A., and Taha, H. E., "On Higher-Order Averaging of Time-Periodic Systems: Reconciliation of Two Averaging Techniques," *Nonlinear Dynamics*, Vol. 99, 2020, pp. 813–836, DOI: https://doi.org/10.1007/s11071-019-05085-4.

[22]Oppenheimer, M. W., Weintraub, I. E., Sighorsson, and Doman, D. B., "Quarter Cycle Modulation of a Minimally Actuated Biomimetic Vehicle," AIAA 2014-1467, Proceedings of the AIAA SciTech Forum, National Harbor, MD, January 13–17, 2014, DOI: https://doi.org/10.2514/1.G000548.

[23]Oppenheimer, M. W., Weintraub, I. E., Sighorsson, and Doman, D. B., "Control of a Minimally Actuated Biometric Vehicle Using Quarter-Cycle Wingbeat Modulation," *Journal of Guidance, Control, and Dynamics*, Vol. 38, (7), 2015, pp. 1187–1196, DOI: https://doi.org/10.2514/1.G000548.

[24]Sigthorsson, D. O., Oppenheimer, M. W., and Doman, D. B., "Flapping-Wing Micro-Air-Vehicle Control Employing Triangular Waves Strokes and Cycle Averaging," AIAA 2010-7553, Proceedings of the AIAA Guidance, Navigation, and Control Conference, Toronto, Ontario, Canada, August 2–5, 2010, DOI: https://doi.org/10.2514/6.2010-7553.

[25]Sigthorsson, D. O., Oppenheimer, M. W., and Doman, D. B., "Flapping-Wing Micro-Air-Vehicle 4-DOF Controller Applied to a 6-DOF Model," AIAA 2010-7554, Proceedings of the AIAA Guidance, Navigation, and Control Conference, Toronto, Ontario, Canada, August 2–5, 2010, DOI: https://doi.org/10.2514/6.2010-7554.

[26]Finio, B. M., Perez-Arancibia, N. O., and Wood, R. J., "System Identification and Linear Time-Invariant Modeling of an Insect-Sized Flapping-Wing Micro Air Vehicle," Proceedings of the 2011 IEEE/ESJ International Conference on Intelligent Robots and Systems, San Francisco, CA, September 25–30, 2011, DOI: https://doi.org/10.1109/IROS.2011.6094421.

[27]Cheng, D., and Deng, X., "Translational and Rotational Damping of Flapping Flight and Its Dynamics and Stability at Hovering," *IEEE Transactions on Robotics*, Vol. 27, (5), 2011, pp. 849–864, DOI: 10.1109/TRO.2011.2156170.

[28]Lopez, M. J. S., and Prasad, J. V. R., "Linear Time Invariant Approximations of Linear Time Periodic Systems," *Journal of the American Helicopter Society*, **62**, 012006 (2017), DOI: 10.4050/jahs.62.012006.

[29]Lopez, M. J. S., "Linear Time Invariant Approximations of Linear Time Periodic Systems for Integrated Flight and Vibration Control," Ph.D. thesis, Georgia Institute of Technology, Atlanta, GA, May 2016.

[30]Saetti, U., and Horn, J. F., "Load Alleviation Flight Control Design Using High-Order Dynamic Models," *Journal of the American Helicopter Society*, **65**, 032009 (2020), DOI: https://doi.org/10.4050/JAHS.65.032009.

[31]Saetti, U., Horn, J. F., Berger, T., and Tischler, M. B., "Handling-Qualities Perspective on Rotorcraft Load Alleviation Control," *Journal of Guidance, Control, and Dynamics*, Vol. 43, (10), 2020, pp. 1792-1804, DOI: https://doi.org/10.2514/1.G004965.

[32]Saetti, U., and Lovera, M., "Time-Periodic and High-Order Time-Invariant Linearized Models of Rotorcraft: A Survey," *Journal of the American Helicopter Society*, **67**, 012008 (2022), DOI: https://doi.org/10.4050/JAHS.67.012008.

[33]Saetti, U., and Rogers, J. D., "Harmonic Decomposition Models of Flapping-Wing Flight for Stability Analysis and Control Design," *Journal of Guidance, Control, and Dynamics*, Vol. 45, (8), March 2022, pp. 1371–1384, DOI: https://doi.org/10.2514/1.G006447.

[34]Pandyan, R., and Sinha, S. C., "Time-Varying Controller Synthesis for Nonlinear Systems Subjected to Periodic Parametric Loading," *Journal of Vibration and Control*, Vol. 7, (1), 2001, pp. 73–90, DOI: https://doi.org/10.1177/107754630100700105.

[35]Colaneri, P., Celi, R., and Bittanti, S., "Constant Coefficient Representation of Discrete Periodic Linear Systems," Proceedings of the Fourth Decennial Specialists' Conference on Aeromechanics, San Francisco, CA, January 21–24, 2004.

[36]Saetti, U., and Rogers, J. D., "Revisited Harmonic Balance Trim Solution Method for Periodically-Forced Flight Vehicles," *Journal of Guidance, Control, and Dynamics*, Vol. 44, (5), May 2021, pp. 1008–1017, DOI: https://doi.org/10.2514/1.G005553.

[37]Corle, K. H. F. M., E., and Schmitz, S., "Time- and Frequency-Domain Whirl-Flutter Analysis using a Vortex Particle Method," Proceedings of the 75th Annual Forum of the Vertical Flight Society, Philadelphia, PA, May 14–15, 2019.

[38]Kokotovic, P. V., O'Malley, R. E., and Sannuti, P., "Singular Perturbations and Order Reduction in Control Theory, an Overview," *Automatica*, Vol. 12, (2), 1976, pp. 123–132, DOI: https://doi.org/10.1016/0005-1098(76)90076-5.

[39]Horn, J. F., "Non-Linear Dynamic Inversion Control Design for Rotorcraft," *Aerospace*, **6**, 38 (2019), DOI: https://doi.org/10.3390/aerospace6030038.

[40]Pitt, D. M., and Peters, D. A., "Theoretical Prediction of Dynamic-Inflow Derivatives," Proceedings of the 6th European Rotorcraft and Powered Lift Aircraft Forum, Bristol, UK, September 16–19, 1980.

[41]Oppenheimer, M. W., Doman, D. B., and Sigthorsson, D. O., "Dynamics and Control of a Biomimetic Vehicle Using Biased Wingbeat Forcing Functions Part I - Aerodynamic Model," AIAA 2010-1023, Proceedings of the 48th AIAA Aerospace Sciences Meeting, Orlando, FL, January 4–7, 2010, DOI: https://doi.org/10.2514/6.2010-1023.

[42]Doman, D. B., Oppenheimer, M. W., and Sigthorsson, D. O., "Dynamics and Control of a Biomimetic Vehicle Using Biased Wingbeat Forcing Functions Part II - Controller," AIAA 2010-1024, 48th AIAA Aerospace Sciences Meeting, Orlando, FL, January 4–7, 2010, DOI: https://doi.org/10.2514/6.2010-1024.

[43]Oppenheimer, M. W., Doman, D. B., and Sighorsson, "Dynamics and Control of a Biomimetic Vehicle Using Biased Wingbeat Forcing Functions," *Journal of Guidance, Control, and Dynamics*, Vol. 34, (1), 2011, pp. 204–217, DOI: https://doi.org/10.2514/1.49735.

[44]Passaro, M., and Lovera, M., "LPV Model Identification of a Flapping wing MAV," Proceedings of the Fourth IFAC Workshop on Linear Parameter Varying Systems, Milan, Italy, July 19–20, 2021.

[45]Sane, S. P., "Induced Airflow in Flying Insects I. A Theoretical Model of the Induced Flow," *Journal of Experimental Biology*, Vol. 209, (1), 2005, pp. 32–42, DOI: https://doi.org/10.1242/jeb.01957.

[46]Ramasamy, M., Lee, T. E., and Leishman, J. G., "Flowfield of a Rotating-Wing Micro Air Vehicle," *Journal of Aircraft*, Vol. 44, (4), 2007, pp. 1236–1244, DOI: https://doi.org/10.2514/1.26415.

[47]Li, H., Burggag, O. R., and Conlisk, A. T., "Formation of a Rotor Tip Vortex," *Journal of Aircraft*, Vol. 39, (5), 2002, pp. 739–749, DOI: https://doi.org/10.2514/2.3020.

[48]Taha, H. E., Tahmasian, S., Woosley, C. A., Nafayeh, A. H., and Hajj, M. R., "The Need for Higher-Order Averaging in the Stability Analysis of Hovering, Flapping-Wing Flight," *Bioinspiration & Biomimetics*, **10**, 016002 (2015), DOI: https://doi.org/10.1088/1748-3190/10/1/016002.

[49]Johnson, W., *Rotorcraft Aeromechanics*, Cambridge University Press, Cambridge, UK, 2013, DOI: https://doi.org/10.1017/CBO9781139235655.

[50]Griffiths, D. A., Ananthan, S., and Leishman, J. G., "Predictions of Rotor Performance in Ground Effect Using a Free-Vortex Wake Model," *Journal of the American Helicopter Society*, Vol. 50, (4), October 2005, pp. 302–314, DOI: 10.4050/1.3092867.

[51]Bhagwat, M. J., and Leishman, J. G., "Generalized Viscous Vortex Model for Application to Free-vortex Wake and Aeroacoustic Calculations," Proceedings of the 58th Annual Forum of the American Helicopter Society, Montreal, Canada, May 11–13, 2002.

[52]van den Berg, C., and Ellington, C. P., "The Vortex Wake of a Hovering Model Hawkmoth," *Philosophical Transactions of the Royal Society B: Biological Sciences*, Vol. 352, (1351), 1997, pp. 32–42, DOI: https://doi.org/10.1098/rstb.1997.0023.

[53]Tarascio, J. M., Ramasamy, M., Chopra, I., and Leishman, J. G., "Flow Visualization of Micro Air Vehicle Scaled Insect-Based Flapping Wings," *Journal of Aircraft*, Vol. 42, (2), Mar–April 2005, pp. 385–390, DOI: https://doi.org/10.2514/1.6055.

[54]Ramasamy, M., Leishman, J. G., and Singh, B., "Wake Structure Diagnostics of a Flapping Wing MAV," *Journal of Aerospace*, Vol. 114, (1), 2005, pp. 907–919, DOI: https://www.jstor.org/stable/44682781.